Parasitic modulation of microwave signals by a hypersonic plasma layer

Nicholas A. Roberds,[a] Matthew W. Young, Nathan E Miller, Caleb Logemann, Tony K. Statom, and Ross M. Wagnild
Sandia National Laboratories, PO Box 5800, Albuquerque, NM 87185, USA

(Dated: 9 August 2023)

During hypersonic flight, compressional and viscous heating of the air can form a plasma layer which encases the aircraft. If the boundary layer becomes turbulent, then the electron density fluctuations can effect a parasitic modulation in microwave signals transmitted through the plasma. We developed an approach for studying the interaction of microwave signals with a turbulent, hypersonic plasma layer. The approach affords a great deal of flexibility in both the plasma layer model and the antenna configuration. We then analyzed a line-of-sight problem in which microwaves, transmitted from a rectangular aperture antenna, propagate through a turbulent plasma layer to a distant receiver. We characterized the first and second order statistics of the computed parasitic modulation and quantified the depolarization of the signal. The amplitude fluctuations are lognormally distributed at low frequencies and Rice distributed at high frequencies. Fluctuations in the co-polarized phase and amplitude of the far field signal are strongly anti-correlated. We used a multi-output Gaussian process (MOGP) to model these quantities. The efficacy of the MOGP model is demonstrated by recovering the time evolution of the co-polarized phase given the co-polarized amplitude and occasional measurements of the phase.

I. INTRODUCTION

During the atmospheric entry of a spacecraft, heating of the surrounding air leading to plasma formation may cause a period of radio blackout. A number of approaches towards mitigating radio blackout have been considered in the past: optimization of the aerodynamic shaping with radio transmission as a constraint, the use of magnetic fields to allow for whistler mode transmission through the plasma and also the use of high frequencies.[1,2] With a high transmission frequency, most of the microwave energy will be transmitted through the plasma layer rather than being reflected or absorbed. Nevertheless, turbulent structures in the plasma layer electron density can modulate a high frequency signal. A better understanding of the high frequency microwave channel characteristics during hypersonic flight is therefore of interest.

To provide context we give a brief, but by no means comprehensive, account of recent work in the literature. Most work regarding radio blackout has been concerned with laminar plasma layers. There have been a few examples of methods where the plasma is modeled as a three-dimensional (3D) reacting Navier–Stokes flow over a realistic geometry and 3D electromagnetic simulations are used to analyze the properties of microwave transmission through the plasma layer.[3,4] Less attention has been given to turbulent plasma layers and the issue of parasitic modulation. He et al. were the first to present a calculation of parasitic modulation given a model for the turbulent plasma layer.[5] In their plasma layer model, turbulent spatial variation is given by a linear eddy model and temporal variation given by a Gaussian random function having a power spectral density consistent with Kolmogorov decay. They characterized the first order statistics of the correlated noise. Shi et al.[6] introduced a novel reduced order model description of parasitic modulation which can be informed by statistical properties of flight conditions. They used a multistate Markov chain to model the microwave channel behavior over a long timescale which includes not only high frequency fluctuations from turbulence but also slower variations due to shifting angle of attack and even slower variation due to descending altitude. Bai et al. considered the statistical properties of the polarization for waves which obliquely propagate through a turbulent plasma layer.[7] Recently, Yao et al. explored the nature of the correlation between amplitude and phase fluctuations, using a slab model for the plasma.[8] In most of the aforementioned work, the historical RAM-C experiments were used to inform the target plasma conditions of calculations and experiments.[9]

Here, we introduce a methodology for studying the parasitic modulation in a microwave signal due to transmission through a turbulent plasma layer. We applied it to a line-of-sight transmission problem and obtained a comprehensive characterization of the parasitic modulation. In this work, the plasma layer is modeled with a surrogate description of hypersonic plasma turbulence which has been previously used for aero-optics studies.[10] In the future we intend to analyze high fidelity plasma layer models, such as a large eddy simulation (LES) model, with this methodology.

In section II, we outline the methodology for computing the properties of the parasitic modulation. Then, we explore the line-of-sight propagation of microwave signals transmitted from a rectangular aperture antenna terminating on a flat ground plane in section III. In our analysis, the signal is found to be partially depolarized by interaction with the turbulent plasma layer. We use the cross-polarization discriminate (XPD) to quantify the depolarization. We found that the amplitude experiences lognormal fading at low frequencies and Rice fading at higher frequencies, above the plasma frequency. The Wang-Strohbehn distribution is effective at modeling the amplitude fluctuations at all frequencies considered.[11] In addition, strong correlations between the cross- and co-polarized signal amplitudes and phases are seen. It therefore seems natural to model these quantities of interest as a multi-output Gaussian process (MOGP). We demonstrate

[a]Electronic mail: nroberd@sandia.gov

the efficacy of this approach by recovering, with high accuracy, the time evolution of the co-polarized phase given the cross- and co-polarized amplitudes as well as occasional measurements of the co-polarized phase. Closing discussion is then provided in section IV.

II. METHOD FOR CALCULATING THE PARASITIC MODULATION

The hypersonic motion of turbulent flow structures across an antenna aperture is far slower than the transit of microwave energy through the plasma layer; the RAM-C2 experiment reached a maximum velocity of around 7500 m/s during atmospheric entry. We therefore treat the plasma profile as being quasi-stationary when solving Maxwell's equations. This approximation is to consider relativistic effects in the frequency broadening as negligible,[12] and the plasma electron response to the microwaves as linear. For our approach, then, we need a number of instantaneous frames f_i, $i \in [1,N]$ describing the 3D plasma profile at successive moments in time.

The method proceeds by processing the sequence of frames. For each frame we compute the time-domain transmission of a microwave pulse, radiated by some antenna structure, through the plasma. The shape of the pulse can be selected to excite a microwave spectrum of interest. The plasma response is accounted for with a linear model for a cold, isotropic plasma. The relative electric permittivity is,

$$\varepsilon_r = 1 - \frac{\omega_\mathrm{p}^2}{\omega(\omega - i\nu)}, \tag{1}$$

where ω_p is the plasma frequency and ν is the electron collision frequency. In future studies, it may be of interest to consider a different linear plasma model, such as a magnetized plasma model.

The electromagnetic calculations are performed with the Empire plasma physics code.[13] Empire implements a conforming finite element time-domain method for electromagnetics. This discretization ensures that the divergence of the magnetic field is zero as long as that condition is met at time zero. The finite element formulation allows a great deal of flexibility in the geometric specification of the antenna, ground surface and plasma layer. Time integration in Empire is implicit. This enables computationally efficient integration of the solution even when the peak plasma frequency and/or collision frequency of the plasma profile is much higher than the microwave frequencies of interest. For details on the Empire numerical method, the reader is referred to the recent work of McGregor et al.[14,15]

Once the electromagnetic response of each frame is computed, the raw solution data is aggregated for analysis. The preprocessing, calculation of the electromagnetic properties of each frame and aggregation of the raw electromagnetic results is orchestrated by a workflow utility called vvtest.[16] In seeking appropriate hypersonic plasma data f_i with which to characterize the signal propagation, one must bear in mind the two key parameters: the total number of frames N and the frame interval ΔT. The total number of frames N should be sufficient to obtain an adequate estimation of statistical properties of the signal, given the selected ΔT. An appropriate value for ΔT may be determined by an estimation of the maximum frequencies present in the power spectral density of the signal or by phase unwrapping considerations.

The frames f_i, containing the electron density and collision frequency profile snapshots, are given by a file in CFD General Notation System (CGNS) format. The CGNS file format is a standard used by contemporary computational fluid dynamics (CFD) codes including, e.g., SPARC.[17]

To load the plasma profile into Empire, we must obtain the plasma state at the finite element quadrature points. This is accomplished in two steps. First, we use a Galerkin projection onto the Empire nodal finite elements ϕ_i. Then nodal finite element interpolation is used to obtain the values of the plasma frequency and electron collision frequency at quadrature points.

The nodal finite element coefficients $\hat{u}_i$ corresponding to some function u by Galerkin projection satisfy,

$$\sum_j M_{ij}\hat{u}_j = f_i, \tag{2}$$

where M_{ij} are elements of the nodal mass matrix. The quantity on the right-hand side (RHS) is,

$$f_i = \int_{\mathcal{V}} \phi_i u \, dV, \tag{3}$$

where $\mathcal{V}$ is the Empire computational domain. The reader is referred to Karniadakis and Sherwin for a rigorous treatment of the projection of a function onto a nodal finite element basis.[18] The quantity u to be projected can represent the plasma frequency or electron collision frequency data given by a CGNS file. The file could be output from a CFD code or it could have been generated by some other means.

Assembly of the RHS quantities f_i is a key task in computing the Galerkin projection. Towards this, we expect u to be given by the CGNS file as a piecewise constant quantity over a hexahedral structured mesh,

$$u(\boldsymbol{x}) = u_i \ : \ \boldsymbol{x} \in \mathcal{C}_i, \tag{4}$$

where $\mathcal{C}_i$ denotes the i$^{\text{th}}$ CGNS mesh element. This is typical for output from a finite volume CFD code. On the other hand, a nodal basis function ϕ_i is compactly supported over a region $\mathcal{E}_i$ coinciding with one or several Empire tetrahedral or hexahedral mesh elements. Therefore the RHS quantities can be expressed,

$$f_i = \sum_j \Big(\int_{\mathcal{V}_{ij}} \phi_i u_j \, dV \Big). \tag{5}$$

Most of the intersections of the CGNS and Empire mesh elements, $\mathcal{V}_{ij} = \mathcal{E}_i \cap \mathcal{C}_j$, will be zero. To identify which $\mathcal{V}_{ij}$ may be non-zero, the domain is decomposed by recursive octree partitioning. At each decomposition level, a bounding estimate for which CGNS and Empire elements are within a given partition is obtained by bounding box testing. Recursion terminates when the number of CGNS/Empire mesh cell pairs

i, j in a partition is less than a specified value. Then, pairs i, j for which $\mathcal{V}_{ij} = 0$ are identified by bounding box tests and eliminated from consideration. Finally, the R3D library is used to compute the intersections of the CGNS and Empire mesh elements, $\mathcal{V}_{ij} = \mathcal{E}_i \cap \mathcal{C}_j$ which may be non-zero.[19]

For the present, we only use linear nodal basis functions which have the property,

$$\int_{\mathcal{V}_{ij}} \phi_i(\boldsymbol{x})\, dV = \phi_i(\bar{\boldsymbol{x}}_{ij}) V_{ij}, \tag{6}$$

where,

$$V_{ij} = \int_{\mathcal{V}_{ij}} dV \tag{7}$$

$$\bar{\boldsymbol{x}}_{ij} = \frac{1}{V_{ij}} \int_{\mathcal{V}_{ij}} \boldsymbol{x}\, dV. \tag{8}$$

The R3D library provides functionality for computing both V_{ij} and $\bar{\boldsymbol{x}}_{ij}$ given $\mathcal{V}_{ij}$. With these simplifying assumptions, the expressions for the RHS quantities reduce to,

$$f_i = \sum_j u_j \phi_i(\bar{\boldsymbol{x}}_{ij}) V_{ij}. \tag{9}$$

And from Eq. 2 the Galerkin projection coefficients are,

$$\hat{u}_i = \sum_j M_{ij}^{-1} f_j. \tag{10}$$

Importantly, we recommend that a practical implementation use the lumped (row-summed) mass matrix to avoid the appearance of significant spurious oscillations in the projection.

With this approach, the loading result will vary in a smooth and well-defined way as the relative spatial resolutions of the CGNS and Empire meshes are varied. The only assumption we make, regarding the CGNS and Empire meshes, is that they at least partially overlap. We note that a naive approach to profile loading, such as nearest point interpolation, will generally produce a corrupted result since turbulent plasma data may not be smoothly varying over any of the length scales associated with the Empire mesh.

III. LINE-OF-SIGHT PROBLEM

One aspect of antenna performance that we can study with our methodology is the line-of-sight propagation of transmitted signals to a distant receiver. Specifically, we will consider the properties of the electric far field along the axis of an aperture antenna,

$$\boldsymbol{E}_i(\boldsymbol{x}_\mathrm{F}, t) = E_{x,i}(\boldsymbol{x}_\mathrm{F}, t)\hat{e}_x + E_{y,i}(\boldsymbol{x}_\mathrm{F}, t)\hat{e}_y, \tag{11}$$

where $\hat{e}_x$ and $\hat{e}_y$ are the x- and y-direction unit vectors, the point $\boldsymbol{x}_\mathrm{F}$ lies on the axis of the antenna waveguide in the far zone and the subscript i denotes the frame number. A near to far field transformation, which computes the time-domain far fields,[20] was used to compute $\boldsymbol{E}_i(\boldsymbol{x}_\mathrm{F}, t)$ from the 3D electromagnetic solution for frame i.

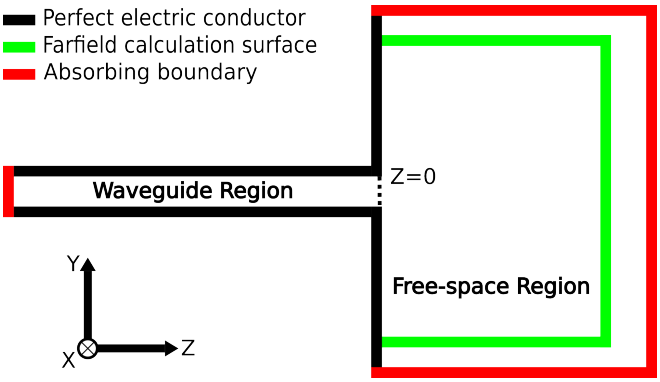

FIG. 1. A cross-sectional view of the problem geometry. The edges are color-coded according to the boundary conditions used in the electromagnetic problem.

A. Electromagnetic problem specification

The problem geometry and electromagnetic boundary condition placement is illustrated in Fig. 1. It is useful to consider the problem domain as the union of two regions. The region $z < 0$ is the waveguide region and $z > 0$ is the free space region. The electric permittivity within the free space region is given by the plasma model, Eq. 1, while the waveguide region has vacuum electrical properties.

Perfect electrical conductor boundary conditions apply to the waveguide walls and the ground surface at $z = 0$. The free space region is bounded by an absorbing boundary condition. There is also an absorbing boundary at the negative-z end of the waveguide, $z = -L$. The free space region contains a 5-sided open cube surface called the near field surface. The near field surface is not associated with any boundary condition, but it is used by the near to far field transformation in computing the electric far field, Eq. 11. The near field surface is sized so that it encloses nearly all electric currents in the problem. It extends out to $z = 9$ cm, which is beyond the extent of the plasma layer.

The antenna waveguide runs along the z-axis from $z = -L$, where $L = 12 l_0$, and terminates at the ground plane $z = 0$. The waveguide cross-section is rectangular with widths $a = l_0$ and $b = 2l_0/3$ in the x and y-directions, respectively. The characteristic length l_0 is defined in terms of the characteristic frequency,

$$l_0 = c/f_0 \tag{12}$$

$$f_0 = 20\ \mathrm{GHz}, \tag{13}$$

where c is the speed of light.

The value of f_0 partially determines the frequency band driven in the electromagnetic problem. For each of the N frames, a simulation is run where the rectangular aperture antenna is driven by a TE_{10} sine-modulated Gaussian pulse. Within the waveguide region, the initial value of the axial,

parallel magnetic field is,

$$\hat{H}_z(z) = \exp\left(\frac{-(z+L/2)^2}{2\sigma_z^2}\right)\sin\left(k_0(z+L/2)\right)$$
$$\hat{H}_z(z) \equiv H_z(z\,;\, x=0, y=0, t=0), \tag{14}$$

where $\sigma_z = l_0$ and $k_0 = 2\pi/l_0$. This fully specifies the initial fields of the pulse; for a TE_{10} eigenmode, the parallel magnetic field, H_z, as well as the transverse electric and magnetic fields, E_y and H_x, can be expressed in terms of $\hat{H}_z$.[21]

The computational mesh for the electromagnetic calculation is a nearly uniformly spaced hexahedral mesh with spacing $\Delta x = l_0/20$. The electromagnetic time step size, $\Delta t = \Delta x/c$, is $\sqrt{3}$ times the explicit Courant-Friedrichs-Lewy limit. The electromagnetic state is evolved for 2.4 ns which is sufficiently long for the total electromagnetic energy to decay over 50 decibels.

An advantage of using a time-domain formulation is that a single simulation run provides results for a wide range of frequencies. Consider the uncertainty principle, $\sigma_z\sigma_k \geq 1/2$ where σ_k is the standard deviation of the pulse wavenumber spectrum. It follows that a narrower pulse (smaller σ_z) is associated with a broader k-space spectrum. A broader k-space spectrum implies a broader temporal frequency spectrum given the form of the TE_{10} mode dispersion relation. The pulse temporal frequency spectrum as well as the pulse axial parallel magnetic field $\hat{H}_z(z)$ used in the present analysis are shown in Fig. 2.

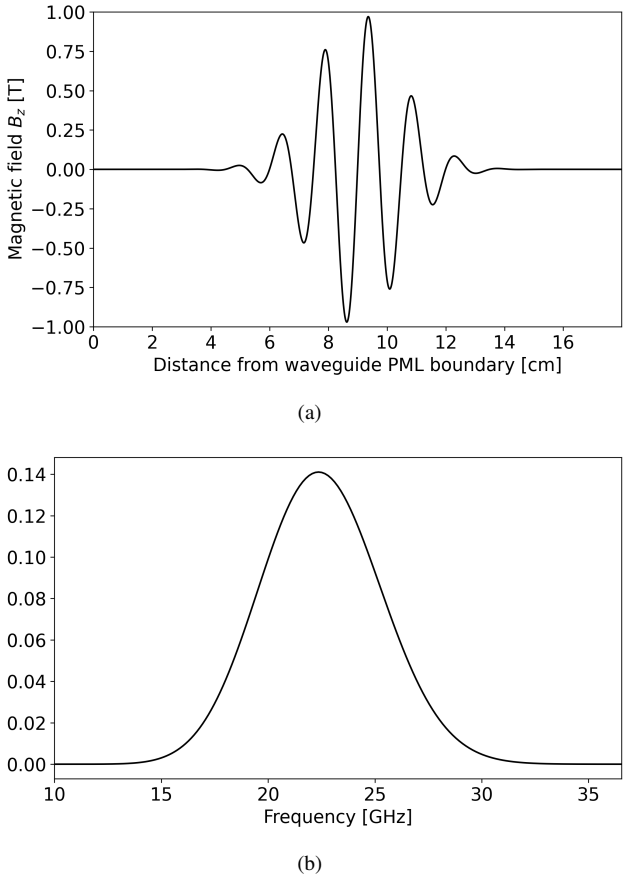

FIG. 2. For each frame, a TE_{10} sine-modulated Gaussian pulse initial condition drives antenna emission. The initial parallel magnetic field along the axis of the waveguide (a) and the pulse spectrum (b) are shown above. The abscissa of the spectrum plot starts at the TE_{10} cutoff frequency for this waveguide. The pulse spectrum is nearly a Gaussian.

B. Plasma layer model

We consider plasma conditions that are representative of the RAM-C2 flight, at 28 km altitude, at a distance $x_0 = 3.5\ d_N$ behind the tip of the nose. The spherically blunted RAM-C2 nose has a diameter $d_N = 12$ in. An interpretation of the RAM-C2 reflectometer readings has suggested that the boundary layer was turbulent at 28 km.[9]

The time-averaged electron density profile is a digitization from figure 14d in Schexnayder et al.[9] The maximum value of the electron density in the time-averaged profile is $n_{\text{peak}} = 7.05\times10^{18}$ m^{-3}, corresponding to a plasma frequency $\omega_{\text{p,peak}} = 2\pi\times 23.7$ GHz. The velocity profile was obtained by a supplemental Reynolds-averaged Navier–Stokes calculation. The time-averaged electron density and velocity profiles are shown in Fig. 3(a).

Turbulent fluctuations in the electron density are modeled as spherical perturbations (*turbules*) superimposed on the time-averaged profile. This model for boundary layer turbulence is based on that used by Trolinger and Rose for aero optics.[10] The radii of the spherical fluctuations, Λ, are distributed according to a modified exponential distribution with a characteristic radius Λ_n,

$$P(\Lambda) = \begin{cases} \kappa\exp\left(\dfrac{\Lambda}{\Lambda_n}\right) & \Lambda_{\min} < \Lambda < \Lambda_{\max} \\ 0 & \text{otherwise,} \end{cases} \tag{15}$$

where κ is a normalization constant. The magnitude of a perturbation is related to the fluctuation strength Δn and the perturbation radius,

$$\Delta n' = \begin{cases} \dfrac{\Lambda\Delta n}{5\delta}, & \text{if } \Lambda < \Lambda_n \\ \dfrac{\Lambda_n\Delta n}{5\delta}, & \text{if } \Lambda > \Lambda_n. \end{cases} \tag{16}$$

The centers of the spherical turbules are uniformly distributed over the boundary layer region $0 < z < \delta$. Note that the supplemental calculation which provided the velocity profile also informed the value of the boundary layer thickness, $\delta = 2.5$ cm. At each frame, the positions of turbules are translated downstream according to the value of the plasma velocity profile at the center of each turbule. Each frame contains approximately 10^4 turbules.

The plasma layer model parameters used in the simulations are given in Table I. The values are intended to provide a reasonable representation of the RAM-C flow conditions, although we offer no proof or rigorous justification. Towards characterizing the properties of microwave signal propagation

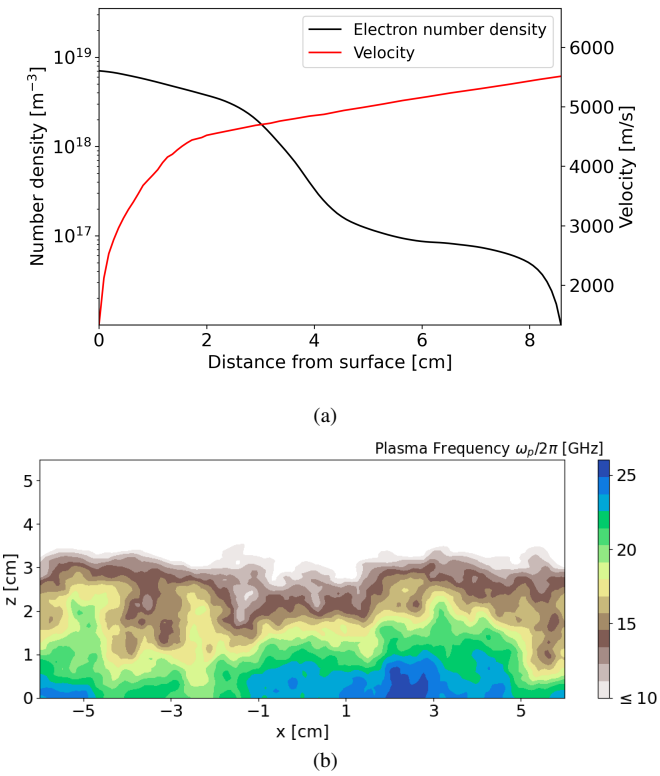

FIG. 3. In (a), the time-averaged electron density and plasma velocity profiles is shown. In (b), a two-dimensional cross-sectional plot of the turbulent plasma frequency is shown.

through a plasma layer model, we ran three series of simulations: $\mathbb{S}_1$, $\mathbb{S}_2$ and $\mathbb{S}_3$. Different random seeds are used to generate the turbules for each series. The plasma layer model parameters are the same for each series, except a different number of frames N and frame interval ΔT are used for $\mathbb{S}_3$. In series $\mathbb{S}_1$ and $\mathbb{S}_2$ there is a strong correlation between subsequent frames due to the small ΔT. These series therefore allow estimation of the second order statistical properties (covariance functions / power spectral densities). The series $\mathbb{S}_3$, having a larger ΔT, provides more information about the first order statistics (probability density functions) of the signal. A cross-sectional plot of the model electron density, at frame $i = 0$ from $\mathbb{S}_1$, is shown in Fig. 3(b).

In addition to the simulation series $\mathbb{S}_1$, $\mathbb{S}_2$ and $\mathbb{S}_3$, we ran simulations for the vacuum and time-averaged plasma cases. The vacuum case is simply the case where there is no plasma. The time-averaged plasma case is the case for which there are no turbulent fluctuations and the plasma profile is just the time-averaged profile shown in Fig. 3(a). These results are useful in the following discussion.

C. Results

First, we consider the polarization of the received signal. It is immediately evident from the transient far field

Simulation series	$\mathbb{S}_1$	$\mathbb{S}_2$	$\mathbb{S}_3$
δ	2.5 cm	-	-
Λ_n	0.2δ	-	-
$\Lambda_{\min}$	0.01δ	-	-
$\Lambda_{\max}$	1.2δ	-	-
Δn	$n_{\text{peak}}/2$	-	-
ΔT	0.75 μs	0.75 μs	5.0 μs
N	2000	2000	3000

TABLE I. Values of the turbulence model parameters used for the line of sight problem. Dashes represent repeated values in a row. The three series of simulations were run with different random number seeds.

at each frame, $\boldsymbol{E}_i(\boldsymbol{x}_{\text{F}}, t)$, that the signal is partially depolarized by scattering from the 3D fluctuations in electron density. The computed cross-polarized component of the far field, $E_{x,i}(\boldsymbol{x}_{\text{F}}, t)$, is non-zero and varying with frame number i when turbulent fluctuations are included. For the vacuum and time-averaged plasma cases, the cross-polarized component is zero. Although the scattering of a plane wave by a single spherical perturbation in ε_r does not induce a cross-polarized field, multiple scattering from many spheres in close proximity is well known to induce a significant cross-polarized field.[22]

To quantify the strength of signal depolarization, we use the cross-polarization discriminate, XPD. The XPD is the ratio of the average cross-polarized spectral intensity to the average co-polarized spectral intensity,

$$XPD(\omega) = 10\log\left(\frac{\langle|\mathscr{E}_{x,i}|^2\rangle}{\langle|\mathscr{E}_{y,i}|^2\rangle}\right), \tag{17}$$

The quantities $\mathscr{E}_{x,i}$ and $\mathscr{E}_{y,i}$ are just the Fourier transforms of the far field components,

$$\begin{aligned}\mathscr{E}_{x,i}(\omega) &= \mathcal{F}[E_{x,i}(\boldsymbol{x}_{\text{F}}, t)]\\ \mathscr{E}_{y,i}(\omega) &= \mathcal{F}[E_{y,i}(\boldsymbol{x}_{\text{F}}, t)].\end{aligned} \tag{18}$$

The computed XPD for simulation series $\mathbb{S}_3$ is plotted in Fig. 4. Peak XPD occurs just below $\omega = \omega_{\text{p,peak}}$. The decrease in XPD with increasing frequency, above $\omega > \omega_{\text{p,peak}}$, occurs because the index of refraction approaches unity at high frequency. Depolarizing scattering interactions with the microwave signal are therefore weaker at higher frequencies.

Next, it will be fruitful to consider the statistical properties of the co-polarized amplitude A and phase ϕ at the receiver,

$$A(t_i\,;\,\omega) = |\mathscr{E}_{y,i}(\omega)| \tag{19}$$

$$\phi(t_i\,;\,\omega) = \text{angle}\big(\mathscr{E}_{y,i}(\omega)\big), \tag{20}$$

where time $t_i = i\Delta T$ and angle is the unwrapped phase angle of the complex-valued argument. The co-polarized amplitude and phase for $f = 26.3$ GHz, over an interval of the $\mathbb{S}_2$ data, is shown in Fig. 5. For all frequencies within the bandwidth of the pulse there is a strong anti-correlation between ϕ and A: the correlation coefficient $\rho \sim -0.7$ in this range. We encountered difficulties in unwrapping the phase between 21 and 25 GHz and attention will be given to this in future work.

Previously, He et al.[5] noted that the amplitude fluctuations follow a lognormal distribution. We fit various models to the

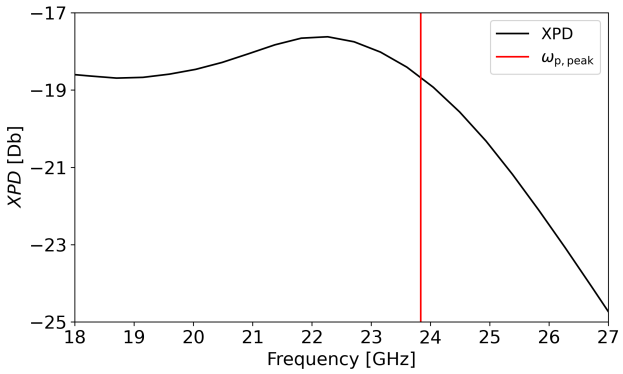

FIG. 4. The cross-polarization discriminate of the far field. The far field signal is most strongly depolarized at a frequency just below the profile peak plasma frequency.

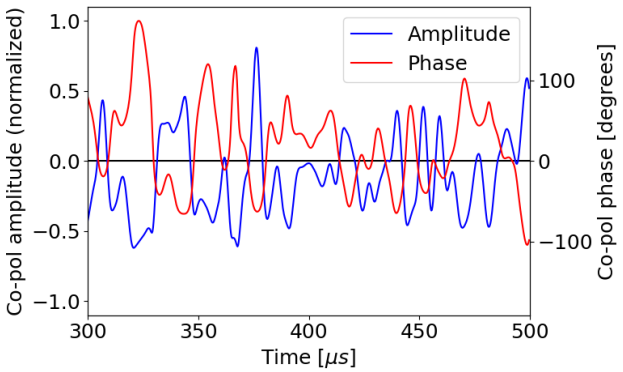

FIG. 5. The computed fluctuations in amplitude and phase, about the mean values, at 26.3 GHz over an arbitrarily selected 200 microsecond interval. It is evident by inspection that there is a strong anti-correlation between these quantities. The strong anti-correlation holds for all frequencies in the pulse bandwidth.

simulation series $\mathbb{S}_3$ data using maximum likelihood estimation. We found that the amplitude is distributed lognormally at lower frequencies. At higher frequencies, however, there is a transition to Rice statistics. In this problem, the transition occurs around $\omega_{\mathrm{p,peak}}$, although further investigation is required to fully understand the transition from lognormal to Rice statistics.

Both the lognormal distribution and Rice distribution have well understood interpretations in line-of-sight signal interference.[23] Lognormal fading arises when the received signal results from multiple scattering along a narrow cone of propagation. Rice signal fading arises when the received signal consists of many uncorrelated scattering contributions. The Rice shape parameter K is the ratio of signal contribution from the direct path to the scattered paths. At low K, the Rice distribution is Rayleigh-like and at high K it becomes Gaussian-like.

In our computed results, the amplitude fluctuations begin to deviate from lognormal statistics at 21 GHz. Amplitude fluctuations follow Rice statistics at 25 GHz and above. In the Rice fading regime, K increases with frequency due to the weaker microwave interaction with the plasma layer for higher frequencies above $\omega_{\mathrm{p,peak}}$. At 25 GHz, $K \approx 0$ corresponding to Rayleigh statistics. At 29.8 GHz, $K = 5.4$, indicating nearly Gaussian statistics.

Wang and Strohbehn proposed the product distribution of a Rice distributed random variable with a lognormally distributed random variable to model the case of many uncorrelated multiple scattering contributions.[11] This distribution can account for a smooth transition from lognormal statistics to Rice statistics. It appears to be highly effective at modeling the amplitude variation statistics in our computed line-of-sight transmission result. However, there is no analytic expression for the probability density function (PDF) so it is cumbersome to work with. Also, this distribution has four model parameters while the Rice and lognormal distributions have only two parameters. A straightforward maximum likelihood estimation procedure for fitting the Wang-Strohbehn distribution to the computed amplitude variation data proved computationally slow and prone to overfitting. Nevertheless, good results were obtained for amplitude variations at all frequencies of interest.

PDFs for some of the fitted models are plotted in Fig. 6. In these plots, an *empirical* PDF is shown for reference. The empirical PDF was obtained by constructing the empirical characteristic function, removing the high frequency noise associated with finite sampling and applying a discrete Fourier transform. In Figs. 6(a) and 6(d), the lognormal and Rice distributions are effective at modeling the data. However, at the transition frequencies of Figs. 6(b) and 6(c) only the Wang-Strohbehn provides a good approximation to the empirical distribution.

The strong correlation between amplitude and phase implies that knowledge of either provides a significant amount of information about the other. A striking demonstration of this can be observed by modeling the phase and amplitude as a multi-output Gaussian random process (MOGP). Gaussian processes are completely defined by the second-order statistics of the signal, viz. the covariance or equivalently the power spectral density.[24] Indeed, the use of random functions is commonplace in the theory of electromagnetic scattering from random media; the covariance of the scattered signal is often a primary quantity of interest.[12]

Given the present model for the turbulent plasma layer, the fluctuations in amplitude and phase can be considered to be stationary random processes. Therefore, their covariance functions can be written as a function of only the lag time. The sample auto- and cross- covariances are thus,

$$\hat{B}_{ij}(\tau_k\,;\,\omega) = \frac{w(\tau_k)}{N-|k|}\sum_{l=1}^{N}\big(q_i(t_{l+k}) - \langle q_i\rangle\big)\big(q_j(t_l) - \langle q_j\rangle\big), \tag{21}$$

where $q_1 = \phi$, $q_2 = A$ and $\tau_k = k\Delta T$ is the lag time. The window function w is selected so that $\hat{B}_{ij}$ will be a more reliable estimate of the covariance B_{ij}; above some maximum correla-

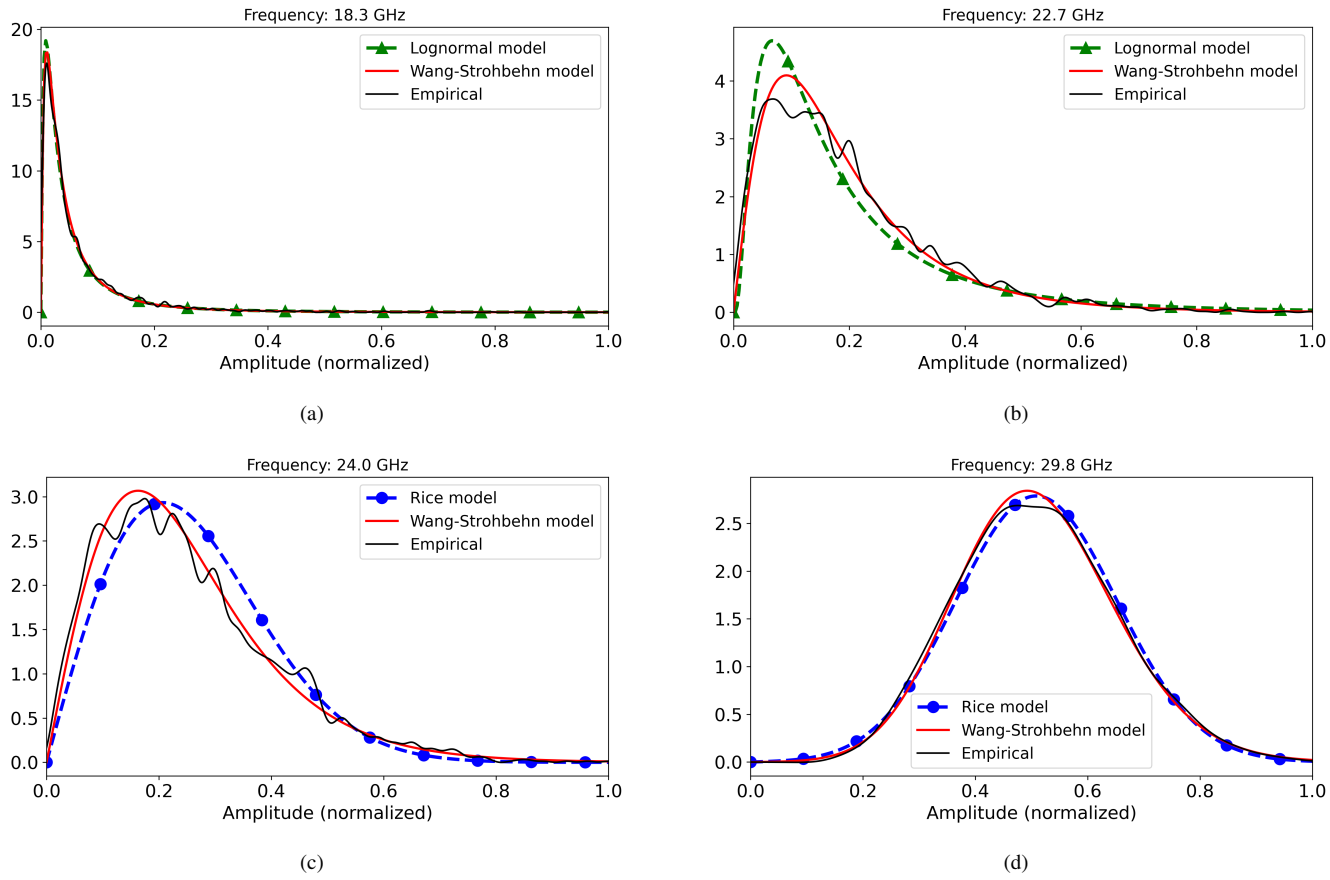

FIG. 6. Estimates for the probability density function of the copolarized amplitude fluctuations. A transition from the lognormal distribution at low frequencies to the Rice distribution at high frequencies can be seen. At intermediate frequencies, (b) and (c), neither the Rice nor lognormal models fit the data well however the Wang-Strohbehn distribution is effective at all frequencies. In each plot, either the Rice or lognormal model is shown according to which model has a higher likelihood for the data.

tion time, it is expected that B_{ij} will be zero. However, as we are estimating the covariances from finite sequences, values for larger τ_k will contain an increasing amount of noise since they result from fewer terms. We use the Tukey window function centered at zero, spanning 40 μs with a Tukey window parameter $\alpha = 0.5$. Therefore, sample covariances are zero for lags $|\tau_k| > 20$ μs.

The sample covariances $\hat{B}_{ij}$ are generally unsuitable for application in Gaussian process modeling; licit covariances are positive-definite functions.[24] A typical approach for estimating a licit auto-covariance is to (hyper-)parameterize the covariance using a functional form which is positive definite (e.g. a Gaussian). One then fits the hyperparameters to, in some sense, approximate B_{ii}. Another approach is to use Bochner's theorem or its multivariate extension to condition the covariance appropriately.[25] Our approach was to simply add independent and identically distributed (iid) noise to the Gaussian process model, following Liu et al.[26] We found that the kriging matrices are well conditioned when a small amount of iid noise is associated with each quantity.

In the following calculations, we estimated the covariances from simulation series $\mathbb{S}_1$ and performed regression on the data from $\mathbb{S}_2$.

Before considering an MOGP model, we first consider a single-output Gaussian process (SOGP) model for the phase. Regression of the phase is performed over an arbitrarily selected 150 μs interval. The SOGP regression is informed by evenly spaced *training* measurements of the computed copolarized phase, $\phi(t\ ;\ \omega = 2\pi \times 26.3\ \text{GHz})$. The training measurements are separated by 10 μs intervals. The result is shown in Fig. 7(a). At each point on the regression interval, SOGP regression provides the posterior probability of the phase as a univariate Gaussian distribution. Both the posterior mean, as well as the region up to one standard deviation away from the mean are indicated in the figure.

If, in addition to the phase training measurements of the copolarized phase, we are given full knowledge of the copolarized amplitude $A(t\ ;\ \omega = 2\pi \times 26.3\ \text{GHz})$, a much more accurate estimation of $\phi(t\ ;\ \omega = 2\pi \times 26.3\ \text{GHz})$ can be obtained with multi-output Gaussian process (MOGP) regression. A multi-output Gaussian process (MOGP) can be considered a vector-valued random function which accounts for the cross-correlations between the different quantities. The result of MOGP regression is shown in Fig. 7(b). In addition

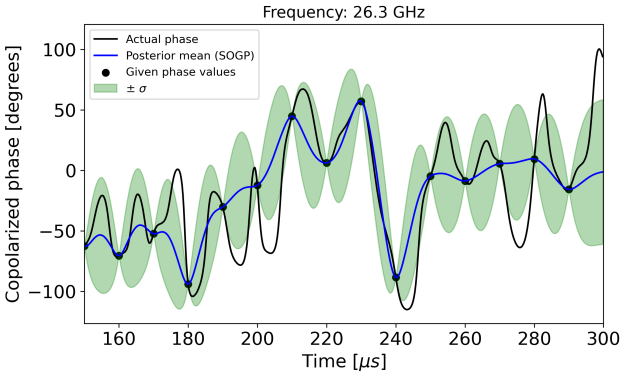

(a)

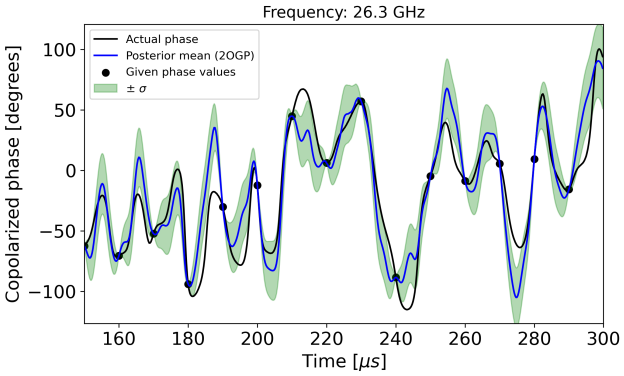

(b)

FIG. 7. Gaussian process regression of fluctuations in the copolarized phase associated with a microwave frequency of 26.3 GHz, which is above the plasma layer peak characteristic frequency of 23.7 GHz. Given training points at which measurements of the copolarized phase are given, (a) single-output Gaussian process and (b) multi-output Gaussian process (MOGP) regression are used. The MOGP regression makes use of the full knowledge of the copolarized amplitude. Because there is a strong correlation between the copolarized phase and amplitude fluctuations, MOGP regression is substantially superior.

to the phase training measurements of the copolarized phase used in the SOGP regression example, the training data includes $A(t\ ;\ \omega = 2\pi \times 26.3\ \text{GHz})$ at every point within the regression interval. It is clear that including knowledge of the amplitude enables a substantially more accurate estimation of the phase. Quantitatively, the L2 error of the SOGP regression result was 9.7% and the MOGP error was 3.6%. For reference, the L2 error of the prior, $\phi(t\ ;\ \omega = 2\pi \times 26.3\ \text{GHz}) = 0$, is 21.5%. We assigned a standard deviation for the iid noise associated with amplitude which is five percent of the standard deviation of the computed fluctuations. The standard deviation of the phase noise was one percent.

We should provide the result of this procedure applied to frequencies below $\omega_{\text{p,peak}}$ as well. The result of MOGP regression at 19.1 GHz is shown in Fig. 8. The L2 error of the result MOGP regression was 3.3% while the L2 error of the

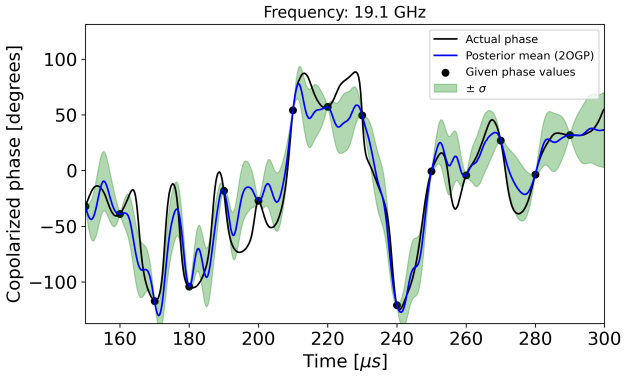

(a)

FIG. 8. MOGP regression of fluctuations in the copolarized phase at 19.1 GHz, which is significantly below the plasma frequency associated with the peak electron density in the layer.

prior was 28.2%. To obtain well conditioned kriging matrices, we had to associate stronger iid noise with the amplitude compared to the 26.3 GHz case: we used ten percent noise for 19.1 GHz. Note that at 19.1 GHz, the amplitude fluctuations are lognormally distributed which contradicts some assumptions of Gaussian process models. At 26.3 GHz, the amplitude statistics are intermediate between Rayleigh and Gaussian, being Rice distributed with Rice shape parameter $K = 1.3$

IV. SUMMARY AND DISCUSSION

An approach to studying the turbulent modulation of microwave signals by re-entry plasma layers, which utilizes 3D electromagnetic simulations, was outlined. In any such study, the specifics of the electron density in the plasma layer is an important aspect. The 3D plasma profile is loaded onto the electromagnetic finite element basis, from a standard CFD file format, by Galerkin projection. It would be straightforward, in principle, to use the results of a high fidelity LES to inform the plasma layer model. Our approach allows for an arbitrary 3D geometry and antenna configuration.

In this work we used a surrogate model for the turbulent plasma layer to study a line-of-sight problem. In the problem, microwaves are transmitted from a rectangular aperture antenna, through the plasma, to a distant receiver. We explored several aspects of the parasitic modulation of the signal by the turbulent plasma layer. First, we noted that the received signal is partially depolarized. This is expected from the basic theory of electromagnetic scattering from random media,[12] although there are few discussions of the phenomenon in this context.

We considered the first order statistics, viz. the probability density function, of the amplitude fluctuations in the line-of-sight problem. We found that the amplitude is lognormally distributed at low frequencies and Rice distributed at high frequencies. The transition from lognormal to Rice statistics, in this case, occurred around the peak plasma frequency of the plasma layer profile. We found that a probability distribution

which can account for a smooth transition from lognormal to Rice statistics, originally proposed by Wang and Strohbehn,[11] was suitable for modeling the amplitude fluctuations at all frequencies considered.

We found that the copolarized phase and amplitude are strongly correlated in the line-of-sight problem. We exploited this by modeling the received signal as an MOGP. An MOGP can serve as a time-domain reduced order model for the parasitic modulation. The MOGP model of the signal proved significantly more effective, in the context of a regression problem, than modeling signal properties individually with SOGPs. The strong correlation between phase and amplitude was found to hold over a wide range of microwave frequencies. Indeed, Yao et al. established that that a strong correlation between phase and amplitude fluctuations, due to a time varying plasma layer, can be generally expected.[8]

The extent to which the computed parasitic modulation reflects reality is limited by the fidelity of the turbulent plasma layer model. The results of the line-of-sight problem presented here should be considered a preliminary effort intended to inform future efforts which consider, say, an LES model of the plasma layer. Although relatively weak depolarization of the signal was computed in the present case, it is reasonable to suspect that a plasma layer having strong spatial anisotropy in the fluctuations could significantly enhance depolarization. Although we observed a transition from lognormal to Rice statistics near the plasma frequency, it is not clear that this should hold generally. Other unforeseen differences, both qualitative and quantitative, could arise when a realistic plasma layer model is considered.

We should note some forseeable ways by which our characterization of parasitic modulation could be improved upon. Future work could identify approaches which are superior to the MOGP as a reduced order model for the signal fluctuations. The amplitude fluctuations are not Gaussian distributed except at high frequencies, which contradicts fundamental assumptions in the Gaussian process model. Towards characterizing the first order statistics of the amplitude fluctuations, we note that the Wang-Strohbehn distribution is difficult to work with for at least two reasons: there is no analytic expression for the probability density function and it has many (four) parameters which can lead to overfitting during maximum likelihood estimation. Finally, we had difficulties in unwrapping the copolarized phase at frequencies near the plasma frequency. We could not manage to unwrap the cross-polarized phase at any frequencies of interest. The lack of computed phase information ultimately limited the scope of our analysis.

ACKNOWLEDGEMENTS

Ed Love and Shane Stafford are recognized for their very helpful advise in developing the CGNS to Empire data loading. We thank Scot Swan for his assistance in developing the automated workflow which made this work possible. This article has been authored by an employee of National Technology & Engineering Solutions of Sandia, LLC under Contract No. DE-NA0003525 with the U.S. Department of Energy (DOE). The employee owns all right, title and interest in and to the article and is solely responsible for its contents. The United States Government retains and the publisher, by accepting the article for publication, acknowledges that the United States Government retains a non-exclusive, paid-up, irrevocable, world-wide license to publish or reproduce the published form of this article or allow others to do so, for United States Government purposes. The DOE will provide public access to these results of federally sponsored research in accordance with the DOE Public Access Plan https://www.energy.gov/downloads/doe-public-access-plan. This paper describes objective technical results and analysis. Any subjective views or opinions that might be expressed in the paper do not necessarily represent the views of the U.S. Department of Energy or the United States Government.

[1] Ryan P Starkey. Hypersonic vehicle telemetry blackout analysis. *Journal of Spacecraft and Rockets*, 52(2):426–438, 2015.

[2] RA Hartunian, GE Stewart, SD Fergason, TJ Curtiss, RW Seibold, et al. Causes and mitigation of radio frequency (RF) blackout during reentry of reusable launch vehicles. Technical report, Aerospace corporation, 2007.

[3] Yusuke Takahashi. Advanced validation of cfd-fdtd combined method using highly applicable solver for reentry blackout prediction. *Journal of Physics D: Applied Physics*, 49(1):015201, 2015.

[4] Madhusudhan Kundrapu, John Loverich, Kristian Beckwith, Peter Stoltz, Alexey Shashurin, and Michael Keidar. Modeling radio communication blackout and blackout mitigation in hypersonic vehicles. *Journal of Spacecraft and Rockets*, 52(3):853–862, 2015.

[5] Guolong He, Yafeng Zhan, Jingzhuo Zhang, and Ning Ge. Characterization of the dynamic effects of the reentry plasma sheath on electromagnetic wave propagation. *IEEE Transactions on plasma science*, 44(3):232–238, 2016.

[6] Lei Shi, Yanming Liu, Shuixun Fang, Xiaoping Li, Bo Yao, Lei Zhao, and Min Yang. Adaptive multistate Markov channel modeling method for reentry dynamic plasma sheaths. *IEEE Transactions on Plasma Science*, 44(7):1083–1093, 2016.

[7] Bowen Bai, Yanming Liu, Xiaoping Li, Bo Yao, and Lei Shi. Instantaneous polarization statistic property of EM waves incident on time-varying reentry plasma. *Physics of Plasmas*, 25(6):062101, 2018.

[8] Bo Yao, Lei Shi, Xiaoping Li, Yanming Liu, and Hailiang Wei. Experimental study on correlation between amplitude and phase of electromagnetic wave affected by time-varying plasma by amplitude-modulated radio frequency plasma generator. *Physics of Plasmas*, 28(4):042107, 2021.

[9] Charles J Schexnayder, Paul W Huber, and John S Evans. *Calculation of electron concentration for a blunt body at orbital speeds and comparison with experimental data*. National Aeronautics and Space Administration, 1971.

[10] James Trolinger and William Rose. Technique for simulating and evaluating aero-optical effects in optical systems. In *42nd AIAA Aerospace Sciences Meeting and Exhibit*, page 471, 2004.

[11] Ting-i Wang and John W Strohbehn. Perturbed log-normal distribution of irradiance fluctuations. *JOSA*, 64(7):994–999, 1974.

[12] Akira Ishimaru. *Wave propagation and scattering in random media*, volume 2. Academic Press, NY, 1978.

[13] Matthew T Bettencourt, Dominic AS Brown, Keith L Cartwright, Eric C Cyr, Christian A Glusa, Paul T Lin, Stan G Moore, Duncan AO McGregor, Roger P Pawlowski, Edward G Phillips, et al. EMPIRE-PIC: A performance portable unstructured particle-in-cell code. *Commun. Comput. Phys.*, 2021.

[14] Duncan Alisdair Odum McGregor, Edward Love, and Richard Michael Jack Kramer. The Crank Nicolson time integrator for EMPHASIS. Technical report, Sandia National Lab.(SNL-NM), Albuquerque, NM (United States), 2018.

[15] Duncan McGregor, Edward Phillips, David Sirajuddin, and Timothy Pointon. Variational, stable, and self-consistent coupling of 3D electro-

magnetics to 1D transmission lines in the time domain. *Journal of Computational Physics*, 451:110856, 2022.

[16] Allen C Robinson, Richard R Drake, M Scot Swan, Nichelle L Bennett, Thomas M Smith, Russell Hooper, and George R Laity. A software environment for effective reliability management for pulsed power design. *Reliability Engineering & System Safety*, 211:107580, 2021.

[17] Micah Howard, Andrew Bradley, Steven W Bova, James Overfelt, Ross Wagnild, Derek Dinzl, Mark Hoemmen, and Alicia Klinvex. Towards performance portability in a compressible CFD code. In *23rd AIAA Computational Fluid Dynamics Conference*, page 4407, 2017.

[18] George Em Karniadakis, George Karniadakis, and Spencer Sherwin. *Spectral/hp element methods for computational fluid dynamics*. Oxford University Press on Demand, 2005.

[19] Devon Powell and Tom Abel. An exact general remeshing scheme applied to physically conservative voxelization. *Journal of Computational Physics*, 297:340–356, 2015.

[20] Nicholas A Roberds and Duncan A O McGregor. A transient near to far field transformation method and verification benchmarking procedure. *Submitted to IEEE Transactions on Antennas and Propagation*, 2023.

[21] John David Jackson. *Classical electrodynamics*. Wiley and Sons, 1999.

[22] J Bruning and Yuen Lo. Multiple scattering of EM waves by spheres part II–numerical and experimental results. *IEEE Transactions on Antennas and Propagation*, 19(3):391–400, 1971.

[23] John W Strohbehn, Ting-i Wang, and James P Speck. On the probability distribution of line-of-sight fluctuations of optical signals. *Radio Science*, 10(1):59–70, 1975.

[24] Carl Edward Rasmussen and Christopher KI Williams. *Gaussian processes for machine learning*, volume 2. MIT Press, Cambridge, 2006.

[25] Tingting Yao and Andre G Journel. Automatic modeling of (cross) covariance tables using fast Fourier transform. *Mathematical Geology*, 30:589–615, 1998.

[26] Haitao Liu, Jianfei Cai, and Yew-Soon Ong. Remarks on multi-output Gaussian process regression. *Knowledge-Based Systems*, 144:102–121, 2018.